Int. J. Multiphase Flow Vol. 14, No. 6, pp. 729–747, 1988
Printed in Great Britain.

0301-9322/88 $3.00 + 0.00

NUMERICAL INVESTIGATION OF TWO-PHASE ROTATING FLOW

M. UNGARISH
Computer Science Department, Technion—Israel Institute of Technology, Haifa 32000, Israel

(*Received* 20 *January* 1988; *in revised form* 28 *June* 1988)

Abstract—Finite difference solutions of the two-fluid equations of motion for a particle (droplet)–fluid mixture in a rotating finite axisymmetric cylinder are presented. The numerical method, which can be regarded as an extension of the Harlow & Amsden approach, employs forward time and centred space discretization and treats implicitly the pressure, Coriolis and volume flux terms. The computed flow fields are examined via a detailed comparison to previous analytic approximations, which illuminates both the physical and numerical aspects and the validity of these approximations.

Key Words: numerical solution, finite differences, rotating mixture, centrifugal separation, two-phase flow, two-fluid equations, Ekman layer

1. INTRODUCTION

The flow of a separating two-phase mixture in a centrifugal field is a fascinating subject from both the fundamental and utilitarian outlooks. A basic configuration for the study of some of the essential effects and of the idiosyncratic features which characterize rotating suspensions is sketched in figure 1. The straight cylindrical container, of radius r_0^* and height H^*, rotating with constant Ω^* around its axis of symmetry, z, contains a mixture consisting of a dispersed phase of "heavy" particles (or droplets) within a continuous "light" fluid (the asterisks denote dimensional variables). The initially assumed solid rotation is an obviously non-steady state under the action of the centrifugal buoyancy. This work concerns the complex separative transient motion—driven by that force and counteracted by Coriolis, drag and viscous terms—during which the dispersed phase is basically squeezed from the mixture and concentrated as a sediment layer on the outer wall.

The mathematical framework is provided by the averaged equations of motion (Ishii 1975; Drew 1983), which, upon quite bold closure assumptions, yield a system of non-linear partial differential equations of apparently Navier–Stokes form, as detailed in section 2. The related dimensionless parameters are: the reduced density difference, $\alpha = (\rho_D^* - \rho_C^*)/\rho_C^*$; the (modified) particle Taylor number, $\beta = \frac{2}{9}a^{*2}\Omega^*\rho_C^*/\mu_C^*$; the Ekman number, $E = \mu_C^*/\rho_C^*\Omega^* r_0^{*2}$; the aspect ratio, $H = H^*/r_0^*$; and the initial disperse volume fraction, $\varepsilon_D(0)$. Here subscripts C and D denote the continuous and dispersed phases, ρ^* is the density and a^* is the radius of the dispersed particle. The present study is relevant to the range $|\alpha| \leqslant 1$, $E \ll 1$, $\beta \ll 1$, $H \gg E^{1/2}$, $\varepsilon_D(0) \leqslant 0.5$.

The solution of this formidable theory, subject to "reasonable" boundary conditions, is a multipurpose task. It is expected to: (1) provide physical insight; (2) serve as a simulation of real apparatuses, i.e. accurately predict measurable variables; (3) illuminate the methodology of two-phase flow theory in this physical setting, which is very different from the gravity environment for which the leading assumptions have been tailored and tested. These tasks—and especially the last two—clearly demand accurate results, or, at least, a good estimate of the error bound in the solution. Moreover, due to the skepticism about the presently available closure postulates (discussed later), it is highly desirable to construct solution methods not restricted *a priori* to certain hypotheses. These requirements motivate the numerical solutions of the full two-fluid equations which is the subject of the present investigation. The basic details of the employed finite-difference scheme are presented in section 3.

Conclusions about the flow field are drawn from the numerical results presented in section 4, mostly upon comparison with the analytic solutions of Greenspan (1983) and Ungarish (1986). The former approach, subsequently referred to as G, treats the interior of an *infinitely long* cylinder

(endcaps neglected). On account of this simplification, the two-fluid formulation admits an exact similarity solution where the volume fraction and the velocities divided by the radius are functions of time only, see appendix A. The latter investigation, hereafter denoted as U, tackles the *finite* cylinder via a boundary layer analysis ($E \to 0$, $\beta \to 0$) of the linear flow ($\alpha \to 0$), in the framework of the mixture formulation, see appendix B. It indicates that viscous layers of Ekman type develop on the endplates.† In the interior flow, the most pronounced discrepancies between U and G show up in the azimuthal velocity when the parameter $\lambda = E^{1/2}/|\alpha|\beta H$, which represents the relative importance of the Ekman layers in the angular momentum balance, is not small.‡

The present numerical calculations essentially confirm the above-mentioned analytic predictions, but also provide additional insight and broader understanding of both the applicability and the limitations of these approximations. In general, a comparison indicates a good agreement between numerical and analytical results, which, in turn, increases confidence in the present solver as well as in the previous models.

2. FORMULATION

The time-dependent motion of the two incompressible, immiscible components in a system rotating with a constant $\mathbf{\Omega}^*$ is represented by the averaged flow variables of the continuous and dispersed phases subscripted by C and D, respectively. The appropriate mixture variable is denoted by the subscript m. Some important kinematic relationships between the phase occupancy (or volume fraction) ε_f, mass velocity $\mathbf{q}_f^*$ and volume flux $\mathbf{j}_f^*$ are:

$$\varepsilon_C + \varepsilon_D = 1, \tag{1}$$

$$\mathbf{j}_f^* = \varepsilon_f \mathbf{q}_f^*, \qquad f = \text{D or C}, \tag{2}$$

$$\mathbf{j}_m^* = \mathbf{j}_D^* + \mathbf{j}_C^*. \tag{3}$$

The equations of motion (see Ishii 1975) are:

total volume continuity,

$$\nabla \cdot \mathbf{j}_m^* = 0; \tag{4}$$

dispersed phase continuity,

$$\frac{\partial \varepsilon_D}{\partial t^*} + \nabla \cdot \mathbf{j}_D^* = 0; \tag{5}$$

and

momentum balance,

$$\rho_f^* \left[\frac{\partial \mathbf{j}_f^*}{\partial t^*} + \nabla \cdot \mathbf{j}_f^* \mathbf{q}_f^* + 2\mathbf{\Omega}^* \times \mathbf{j}_f^* \right] = \varepsilon_f [-\nabla P_f^* - (\rho_f^* - \rho_C^*)\mathbf{\Omega}^* \times (\mathbf{\Omega}^* \times \mathbf{r}^*) + \nabla \cdot \tilde{\tau}_f^*] + \mathbf{M}_f^{*d}, \quad f = \text{D or C}. \tag{6}$$

Here the averaged pressure p_f^* has been reduced as follows:

$$P_f^* = p_f^* - \tfrac{1}{2}\rho_C^* [\mathbf{\Omega}^* \times \mathbf{r}^*]^2, \tag{7}$$

$\tilde{\tau}_f^*$ is the total average stress tensor and $\mathbf{M}_f^{*d}$ is the generalized interfacial drag.

To close the foregoing formulation, constitutive relationships for $\mathbf{M}_f^{*d}$, $P_D^* - P_C^*$ and $\tilde{\tau}_f^*$ should be introduced. A detailed discussion of the difficulties and dilemmas encountered in this task is given by Drew (1983). The constitutive equations adopted in the present work were chosen for their simplicity, proper reduction to the limiting case $\varepsilon_D = 0$, analogy with a homogeneous fluid, consistency with accepted "mixture" formulation and minimization of (practically unknown)

†Actually, no analytic investigation of the two-fluid Ekman layer is available. The related steady von Karman flow studied by Ungarish & Greenspan (1983) hinted at the appearance of a sublayer in which the axial derivative of ε_D is large.

‡The notations α and ε of G and U have been interchanged in the present paper to meet the new style requirements of this journal.

correlation or correction coefficients. The analysis of the resulting finite-difference formulation and, especially, of the calculated flow field does not indicate any apparent flaw, difficulty or aphysical feature which can be either attributed to the particular postulates introduced below or completely obviated by an alternative selection.

The drag terms represent internal interphase forces, whose resultant on the mixture scale vanishes, i.e.

$$\mathbf{M}_C^{*d} + \mathbf{M}_D^{*d} = 0. \tag{8}$$

Since the Stokes formula is expected to reproduce the drag on dispersed particles at least for small β [see the discussion by Ungarish & Greenspan (1984)], and accounting for [8], let

$$\mathbf{M}_D^{*d} = -\mathbf{M}_C^{*d} = -D(\varepsilon_D)\varepsilon_D \frac{9}{2}\frac{\mu_C^*}{a^{*2}}(\mathbf{q}_D^* - \mathbf{q}_C^*), \tag{9}$$

where the correction factor $D(\varepsilon_D)$, assuming that the maximal packing ratio equals 1, is given by the correlation suggested by Ishii & Zuber (1979),

$$D(\varepsilon_D) = (1 - \varepsilon_D)^{-2.5}. \tag{10}$$

Numerical stability considerations impose some limitations on this formula when $\varepsilon_D \to 1$, as discussed in section 3.3.

Some pertinent details and discussion of plausible assumptions for pressure differences are presented by Drew (1983) and Prosperetti & Jones (1984). For the range of ε_D considered in this work the contact between the particles is probably negligible (except, of course, the sediment layer). In this case, the interfacial "jump" condition for momentum and the incompressibility of each phase motivate the employment of an extended capillary law,

$$P_D^* - P_C^* = \text{const.} \tag{11}$$

For the "viscous" stress terms a Newtonian-like behavior is postulated,

$$\nabla \cdot \tilde{\tau}_f^* = \sigma_f \mu_C^* \nabla^2 \mathbf{q}_f^*, \tag{12}$$

and the correction coefficients are taken here, for simplicity, as $\sigma_f = 1$. This formula is quite obvious for $f = C$. Its employment for the other phase, although warrantable in some circumstances (Ishii 1975), is still waiting for experimental support. However, this postulate is consistent with the stress formula usually applied in the "mixture" formulation (at least in regions of small $\nabla\varepsilon_D$, a condition practically satisfied by the flow field under investigation, as seen below). Drew (1983) mentions that, if the dispersed phase consists of solid particles, it is sometimes assumed that $\tilde{\tau}_D^* = 0$. This limit will be briefly hinted at by taking $\sigma_D = 0.2$ in one of the numerical runs reported in section 6 (note that $\sigma_D = 0$ renders singularity).

The boundary conditions are no-slip, no penetration on solid walls and regularity at the axis of rotation. It is asumed that initially the mixture is in solid rotation, $\mathbf{q}_D = \mathbf{q}_C = 0$, and homogeneously blended, $\varepsilon_D = \varepsilon_D(0) = \text{const.}$† The corresponding initial pressure field is given below. In fact, the no-slip boundary condition for the dispersed phase is not rigorous—especially when particles and droplets tend to slide or roll on solid surfaces, such as the endcaps. Experimental evidence on this behavior is, unfortunately, lacking. However, as indicated by Ungarish & Greenspan (1983), this condition seems to affect in particular a very thin sublayer, whose limited consequences are discussed later. Thus, this no-slip boundary condition is regarded as a plausible premise which can be easily replaced in the present numerical code when an improved one is set forth.

To be more specific, the cylindrical coordinate system (r, θ, z) rotating around z is employed, in which the velocity components read $\mathbf{q}_f = \{u_f, v_f, w_f\}$,‡ and the variables are scaled by the

†This is, in general, a non-trivial state because some separation occurs during the spin-up stage and stirring should be involved to strictly recover these initial conditions.

‡f = D or C for the phases, m for the mixture and R for the relative velocity.

length r_0^* (the outer radius of the cylinder), velocity $|\alpha|\beta\Omega^* r_0^*$ (the typical value of $(\mathbf{q}_D^* - \mathbf{q}_C^*)\cdot\hat{r}$), density ρ_C^* and pressure $\frac{1}{2}\rho_C^*|\alpha|\Omega^{*2}r_0^{*2}$. For the dimensionless variables (without asterisks) one obtains, after some arrangement, the following system:

$$\nabla\cdot\mathbf{j}_m = 0, \tag{13}$$

$$\frac{\partial\varepsilon_D}{\partial t} + \nabla\cdot\mathbf{j}_D = 0, \tag{14}$$

$$|\alpha|\beta\frac{\partial\mathbf{j}_D}{\partial t} + 2\hat{z}\times\mathbf{j}_D = -\frac{\varepsilon_D}{1+\alpha}\nabla P + \mathbf{F}_D, \tag{15}$$

$$|\alpha|\beta\frac{\partial\mathbf{j}_C}{\partial t} + 2\hat{z}\times\mathbf{j}_C = -\varepsilon_C\nabla P + \mathbf{F}_C. \tag{16}$$

Here

$$\mathbf{F}_f = -|\alpha|\beta\mathbf{C}_f + \mathbf{S}_f, \qquad f = \text{D or C}, \tag{17}$$

$$\mathbf{C}_f = \nabla\cdot\mathbf{j}_f\mathbf{q}_f \tag{18}$$

is the convection term and the "source" terms are

$$\mathbf{S}_D = \frac{\varepsilon_D}{1+\alpha}\left(\frac{\alpha}{|\alpha|}\frac{1}{\beta}r\hat{r} - \frac{1}{\beta}D(\varepsilon_D)(\mathbf{q}_D - \mathbf{q}_C) + E\nabla^2\mathbf{q}_D\right) \tag{19a}$$

and

$$\mathbf{S}_C = \varepsilon_C\left[\frac{\varepsilon_D}{\varepsilon_C}\frac{1}{\beta}D(\varepsilon_D)(\mathbf{q}_D - \mathbf{q}_C) + E\nabla^2\mathbf{q}_C\right]. \tag{19b}$$

The task is to compute the time-dependent axisymmetric solution of the system [13]–[19] supplemented by [1]–[3] in the domain $0 < r < 1$, $0 < z < H$, $t > 0$, subject to the above-mentioned boundary and initial conditions. This is attempted via the numerical method presented in the next section. The numerical scheme takes advantage of the elliptic equation for P obtained by applying the divergence operator on the sum of [15] and [16] and accounting for [2] and [13]. The result is

$$\nabla\cdot\left(\frac{\varepsilon_D}{1+\alpha} + \varepsilon_C\right)\nabla P = 2\frac{1}{r}\frac{\partial}{\partial r}r\mathbf{j}_m\cdot\hat{\theta} + \nabla\cdot\left[-|\alpha|\beta(\mathbf{C}_D + \mathbf{C}_C) + \mathbf{S}_D + \mathbf{S}_C\right]. \tag{20}$$

Substituting the initial conditions in the last equation yields

$$P(\mathbf{r}, t=0) = \frac{\alpha}{|\alpha|}\frac{1}{2\beta}\frac{\varepsilon_D(0)}{1+\alpha[1-\varepsilon_D(0)]}r^2 + \text{const.} \tag{21}$$

It is worthwhile to emphasize that the present formulation does not distinguish explicitly between the mixture region and the sediment layer anticipated to develop on $r = 1$, see figure 1. It is expected that the sharp increase of ε_D and the form of $D(\varepsilon_D)$ will prevent relative motion in this layer and consequently provide the appropriate qualitative comportment, including the contact stress which stops the particles in this region. Actually, this models the sediment as a Newtonian fluid, of viscosity μ_C^* (this detail can be readily changed). This approach is advantageous from the numerical standpoint and, in some circumstances, can be justified by theoretical and experimental evidences (see Amberg & Dahlkild 1987). The sediment is reproduced by a smoothly growing ε_D (i.e. there is no jump to the maximal packing), therefore the position of the mixture–sediment interface cannot be sharply located on the numerical grid. These simplifications have little consequences when the main flow is of concern and the sediment layer is thin, but should be carefully reconsidered in other cases.

3. BRIEF DESCRIPTION OF THE NUMERICAL TECHNIQUE

The finite-difference method of Harlow & Amsden (1971) has been quite straightforwardly adapted for the present problem. Although variations of this scheme have already been used in the solution of two-phase flows (e.g. Carver 1984), its implementation in the peculiar domain of rapidly rotating two-fluid flows has not been done or discussed before, to the best of the author's knowledge. It is emphasized that the "full" non-linear time-dependent axisymmetric equations are solved.

3.1. Time discretization and marching

Introduce the superscript "+" to denote the dependent variables at the "new" time instance $t + \delta t$, which should be calculated from the known flow field variables at t (without special notation). Forward time discretization is used, e.g. $\partial\varepsilon/\partial t \rightarrow (\varepsilon^+ - \varepsilon)/\delta t$. The pressure, Coriolis and volume flux terms in the continuity equations are defined implicitly at $t + \delta t$.

The momentum equations [15] and [16] yield

$$\mathbf{j}_D^+ + 2m\hat{z} \times \mathbf{j}_D^+ = -\frac{m\varepsilon_D}{1+\alpha} \nabla P^+ + m\mathbf{F}_D + \mathbf{j}_D \qquad [22]$$

and

$$\mathbf{j}_C^+ + 2m\hat{z} \times \mathbf{j}_C^+ = -m\varepsilon_C \nabla P^+ + m\mathbf{F}_C + \mathbf{j}_C, \qquad [23]$$

where

$$m = \frac{\delta t}{|\alpha|\beta}. \qquad [24]$$

First, an elliptic equation for P^+ is derived. The sum of [22] and [23] relates ∇P^+ to $\mathbf{j}_m^+$. Solving for the latter variable and taking the divergence of the result (see appendix C), accounting for global continuity, [13], yields

$$\frac{1}{r}\frac{\partial}{\partial r} rg \frac{\partial P^+}{\partial r} + (1 + 4m^2)\frac{\partial}{\partial z} g \frac{\partial P^+}{\partial z} = \frac{1}{r}\frac{\partial}{\partial r} r[\hat{r} \cdot \mathbf{F} + 2\hat{\theta} \cdot (m\mathbf{F} + \mathbf{j}_m)] + \frac{\partial}{\partial z}\hat{z} \cdot [(1 + 4m^2)\mathbf{F} + 4m\mathbf{j}_m], \qquad [25]$$

where

$$\mathbf{F} = \mathbf{F}_D + \mathbf{F}_C \qquad [26]$$

and

$$g = \frac{\varepsilon_D}{1+\alpha} + \varepsilon_C. \qquad [27]$$

The boundary conditions of Newmann type, $\hat{n} \cdot \nabla P^+$ for the last equation result from substituting the velocity boundary constraints in [22] and [23] and, in particular, $\partial P^+/\partial r = 0$ at $r = 0$. This defines P^+ up to an arbitrary constant. Therefore, for uniqueness, P^+ is set to zero at one grid point as detailed below. It is noted in passing that the initial pressured field, [21], is not used in the present scheme.

After calculating P^+ the components of $\mathbf{j}_D^+$ and $\mathbf{j}_C^+$ are obtained by straightforward substitution into [22] and [23] and employment of [C.1] and [C.2] of appendix C. Subsequently, [14] and [1] yield

$$\varepsilon_D^+ = \varepsilon_D - \delta t \nabla \cdot \mathbf{j}_D^+ \qquad [28]$$

and

$$\varepsilon_C^+ = 1 - \varepsilon_D^+, \qquad [29]$$

and the "new" velocity field follows readily:

$$\mathbf{q}_f^+ = \frac{\mathbf{j}_f^+}{\varepsilon_f^+}, \qquad f = \text{D or C.} \tag{30}$$

This completes, essentially, the calculation of the flow field at $t + \delta t$, and an additional time step can be attempted. It is quite obvious that the major computational effort should be dedicated to the solution of [25].

3.2. *Spatial discretization*

Central differencing on the staggered grid sketched in figure 2 is used. The indexes i, j denote the center of the numerical cell, and the discretized variables are defined at the following points: the volume fractions ε_f and the pressure P—at (i, j); the radial and azimuthal components of the flux and velocity, $(\varepsilon_f u_f)$, $(\varepsilon_f v_f)$, u_f, v_f—at $(i \pm \frac{1}{2}, j)$; the axial components, $(\varepsilon_f w_f)$, w_f—at $(i, j \pm \frac{1}{2})$. Intermediate values are calculated by linear interpolation, and the convection terms are discretized by the ZIP approach (see Harlow & Amsden 1971). The radial intervals δr are constant. To facilitate Ekman layer resolution, an axial stretching $z_j = z(Z_j)$ is introduced such that δZ is constant and $\delta z_j \triangleq z'(Z_j)\delta Z$ (see Toren & Solan 1979). Dummy cells are added for straightforward implementation of boundary conditions, e.g. $u_{i,1} = -u_{i,2}$ and $(\partial u/\partial z)_{i,3/2} \triangleq (u_{i,2} - u_{i,1})/\delta z_{3/2}$ for the boundary $z = 0$ where $j = 3/2$ (it is noted in passing that the formal $O(\delta z^2)$ accuracy is lost in discretized derivatives at the boundary). The finite-difference method is illustrated by the discrete form of [25] at the point (i, j),

$$\frac{1}{r_i}\frac{1}{\delta r}\left[r_{i+(1/2)}g_{i+(1/2),j}\frac{1}{\delta r}(P^+_{i+1,j} - P^+_{i,j}) - r_{i-(1/2)}g_{i-(1/2),j}\frac{1}{\delta r}(P^+_{i,j} - P^+_{i-1,j})\right]$$

$$+\frac{1+4m^2}{\delta z_j}\left[g_{i,j-(1/2)}\frac{1}{\delta z_{j+(1/2)}}(P^+_{i,j+1} - P^+_{i,j}) - g_{i,j-(1/2)}\frac{1}{\delta z_{j-(1/2)}}(P^+_{i,j} - P^+_{i,j-1})\right] = (\text{r.h.s})_{i,j}, \tag{31}$$

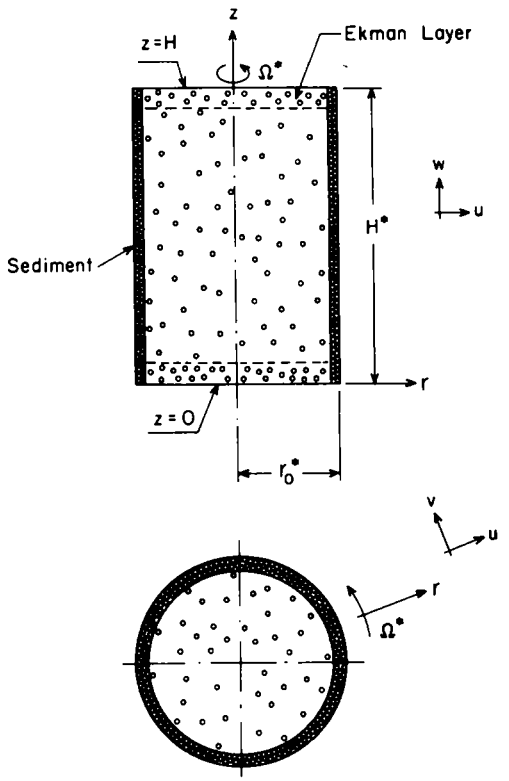

Figure 1. Description of the system.

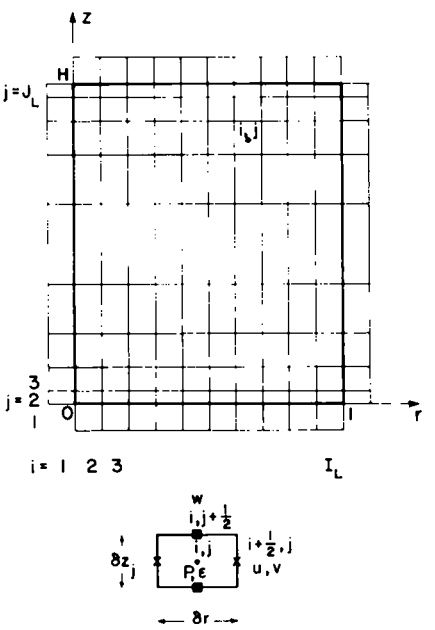

Figure 2. Spatial grid.

where, according to [27],

$$g_{i+(1/2),j} = \frac{1}{2}\left[\frac{1}{1+\alpha}(\varepsilon_{D_{i+1,j}} + \varepsilon_{D_{i,j}}) + (\varepsilon_{C_{i+1,j}} + \varepsilon_{C_{i,j}})\right] \text{ etc.} \quad [32]$$

Equation [31] yields a block tridiagonal system for the unknowns $P^{+}_{i,j}$ at the internal mesh points, $2 \leqslant i \leqslant I_L, 2 \leqslant j \leqslant J_L$ (except $P_{2,2} = 0$), which is solved by direct block factorization [see, for instance, Issacson & Keller (1966)]. This requires about $3(J_L * I_L^3)$ operations per time step. The number of operation in the subsequent computations of the "new" flow variables at the mesh points is proportional to $14(I_L * J_L)$ (volume fraction and three flux and velocity components for each phase).

3.3. Resolution and stability considerations

A comprehensive analysis of the numerical error and stability restrictions is beyond the scope of the present paper. Some pertinent indications on these issues are gained and discussed rather heuristically via the examples presented in section 4.

However, two critical demands should be formulated for understanding some of the numerical challenges encountered in the range of parameters of this investigation. First, the spatial resolution requirements are considered. Shear regions of radial scales $(H\mathrm{E}^{1/2})^{1/2}$ and $(H\mathrm{E})^{1/3}$ are anticipated near the outer sediment layer, and δr should be restricted accordingly. However, when $H \sim 1$, the thinner yet more active Ekman layers dominate. These layers are expected to develop on the endplates ($z = 0, z = H$) and their axial width is $\sim 3\mathrm{E}^{1/2}$. Even a rough resolution of these critical shear regions imposes the limitation $\delta z < \mathrm{E}^{1/2}$. (A simple test model with mesh points at $0.6\mathrm{E}^{1/2}$, $1.8\mathrm{E}^{1/2}$ and $3\mathrm{E}^{1/2}$ overestimates the volume flux in the layer by about 16% due to discretization errors.)

Next, the various plausible time scales encountered in the flow under investigation, as summarized in table 1, are recalled. Thus, since the shortest time scale in this problem is probably the relaxation interval, $\sim|\alpha|\beta^2$, a smaller δt is needed for reproducing it. Although the relaxation behavior decays exponentially after $t = 0$, the appropriate balance, which is essentially

$$|\alpha|\beta\frac{\partial u_D}{\partial t} \approx -\frac{D(\varepsilon_D)}{\beta}u_D, \quad [33]$$

prevails. Moreover, the corresponding stability restriction

$$\delta t < \frac{|\alpha|\beta^2}{D(\varepsilon_D)} = |\alpha|\beta^2(1-\varepsilon_D)^{2.5} \quad [34]$$

becomes eventually more severe due to the continuous increase of $\varepsilon_D \to 1$ in the sediment region. (This limitation strongly suggest treating the drag terms implicitly, which, however, considerably complicates the scheme.) To avoid prohibitively small δt resulting from [34], the value of $D(\varepsilon_D)$ is artificially chopped to 10 when [34] yields larger values. Thus, to simulate the process during the separation interval ~ 1, about $10/(|\alpha|\beta^2)$ time steps should be calculated. From the physical standpoint, this setting of $D(\varepsilon_D)$ captures the limited relative

Table 1

Process	Time scale	
	Dimensional	Dimensionless
Particle relaxation (for buoyancy–drag balance)	$a^{*2}\frac{\rho_D^*}{\mu_C^*}$	$(1+\alpha)\lvert\alpha\rvert\beta^2$
Revolution of system, development of Ekman layers, inertial oscillations	Ω^{*-1}	$\lvert\alpha\rvert\beta$
Spin-up	$H^*\sqrt{\frac{\rho_C^*}{\mu_C^*\Omega^*}}$	$\frac{1}{\lambda}$
Phase separation	$(\lvert\alpha\rvert\beta\Omega^*)^{-1}$	1
Viscous momentum diffusion	$H^{*2}\frac{\rho_C^*}{\mu_C^*}$	$\frac{1}{\lambda\mathrm{E}^{1/2}}$

motion in the sediment but does not account for dominant contact stress or coalescence. The subsequent comparison to theory vindicates the assumption that the details in this layer have little influence on the external flow when $\varepsilon_D(0)$ is not large.

4. RESULTS

Numerical solutions were obtained for the two cases:

$$\text{(I) } \alpha = 0.5; \qquad \text{(II) } \alpha = 0.1.$$

The other parameters in both systems are

$$E = 0.01, \quad \beta = 0.1, \quad H = 2 \quad \text{and} \quad \varepsilon_D(\mathbf{r}, t = 0) = 0.2.$$

Note that $\lambda = 1$ and $\lambda = 5$ in cases I and II, respectively.

The computations were carried out until $t = 1.0$ at least, which is believed to cover the most significant aspects of the flow field behavior.

The subsequent discussion concerns mostly, and unless otherwise mentioned, the results of the following discretization. The numerical grids contain 10 equal radial intervals and 10 stretched axial spacings ($z_j = \{0.0496, 0.172, 0.333, 0.546, 0.827, 1.173, 1.454, 1.667, 1.828, 1.9504\}$) and the time step is $\delta t = 10^{-4}$.† Here the required computer resources for single precision arithmetic, are, approx. 50,000 words of memory and, per time step, 0.029 s CPU on a CRAY X-MP/48‡ or 0.21 s CPU on an IBM-3081 D§ (it is recalled that the single precision calculation on the former computer uses more significant digits than the latter, but no critical discrepancies seem to show up in the present runs). The results on the coarse grid are emphasized because their display and analysis is simpler and their reproduction is affordable on medium-sized computers. Moreover, their accuracy seems satisfactory for both engineering and scientific applications, except for small details as discussed below.

In addition, some reference will be made to solutions under finer spatial and time discretization, in particular, using 30 stretched axial intervals.

The overall observed features of the flow field are, roughly, as follows. The heavier phase D is expelled radially by the centrifugal buoyancy which, after a short relaxation interval, is counteracted by drag and Coriolis terms. The main result is a quasi-steady radial relative velocity, $u_R \propto r$, accompanied by a similar u_D. The volume fraction ε_D therefore continuously decreases in the main mixture bulk but increases near the outer wall (the "sediment layer") where the radial motion is blocked. A retrograde azimuthal motion, $v_m < 0$, is induced by the radial migration of the heavier phase in account of angular momentum conservation. The viscous frictional effects on the endcaps, which attempt to reduce the above-mentioned angular lag, are mostly confined to boundary layers of Ekman type. These layers absorb mixture from the interior, transport it to larger radii and eject it axially near the outer wall. (This "spin-up" secondary circulation is closed by an inwardly radial small volume flux in the inviscid core.) The positive u_R gives rise to a small negative azimuthal relative velocity, $v_R < 0$. The details are discussed below.

Consider system I (i.e. $\alpha = 0.5$).

First, the results for ε_D are analyzed. Figure 3a shows that near the midplane $z = 1$ this variable is (almost) independent of r (except the sediment layer). The typical z dependence of this variable can be inferred from figure 3c, based on the 10×30 mesh results (with $\delta t = 5 \times 10^{-5}$). It is observed that ε_D has a sharp axial variation in a sublayer‖ whose characterstic thickness is $\sqrt{E\beta}$ ($\approx$one particle radius in dimensional form). Near the endplate the initial value of 0.2 essentially prevails. This peculiar sublayer comportment confirms the analytical results obtained for the related von Karman rotating two-phase boundary layer by Ungarish & Greenspan (1983). Further discussion of this region is given below, when the results for the strongly related relative

†In run (II), $\delta t = 0.8 \times 10^{-4}$, for $t > 0.7$, was used to overcome numerical instabilities.

‡When no special vectorization tools or strategy is used. An additional speedup factor of about 2 result upon employment of the CRAY routine MINV for the inverse of a matrix instead of the IMSL routine LINV1F.

§Using highest optimization on compiler VS-Fortran.

‖The term sublayer is used to stress the thinness as compared to the more common Ekman layers which form on the plates.

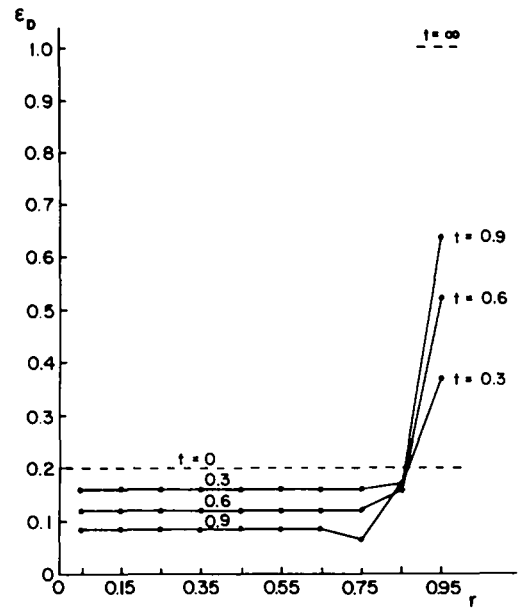

Figure 3a. ε_D vs r at various times; $\alpha = 0.5$. (Numerical results at "midplane" $z = 0.827$.)

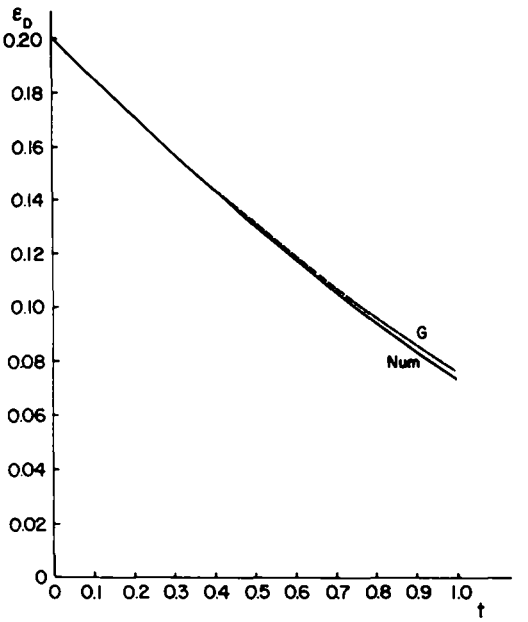

Figure 3b. ε_D vs t in the core; [Numerical results at (0.05, 0.827).]

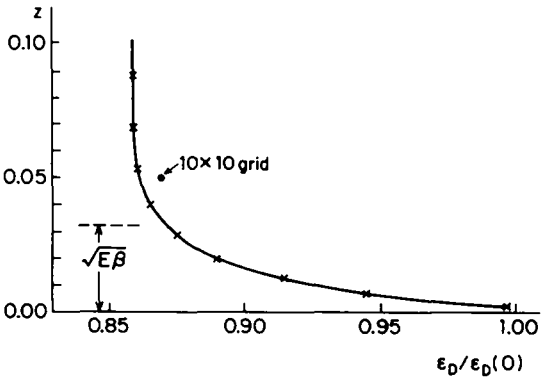

Figure 3c. $\varepsilon_D/\varepsilon_D(t = 0)$ vs z in the sublayer, at $t = 0.2$, $r = 0.05$. ×, 10×30 grid (values of z_i can be inferred from the graph); ●, 10×10 grid (at closest point to boundary).

velocity are analyzed. Outside the sublayer, the axial changes of ε_D are usually in the fourth digit. It is noted that the grid 10×10 has only one point across the sublayer. Nevertheless, the accuracy of ε_D in the core is very good as indicated below. It is concluded that, except the thin sublayers, the numerical results are in good agreement with the similarity assumption of G, $\varepsilon_D = \varepsilon_D(t)$ in the interior and the conjecture of U that ε_D is spatially independent in the Ekman layers. Moreover, figure 3b also indicates a very good quantitative agreement: the numerical results are slightly overestimated by the analytical model G; the discrepancy increases in time to about 4% at $t = 1$. It will be argued later that most of this discrepancy can be attributed to the lack of endplate effects in solution G, while the numerical error in ε_D is no more than 1%. As expected, the sediment layer, figure 3a, is "smeared". In addition, non-physical radial oscillations in ε_D are introduced by the numerical treatment of this kinematic shock. These numerical wiggles become eventually more pronounced, as the "jump" between the core and sediment increases. Thus, for $t = 1$, the oscillations are about -2, 8 and -39% at $r_i = 0.55$, 0.65 and 0.75, respectively. No attempt was made to (artificially) damp those oscillations since they apparently have no significant effect on the present investigation. Similar wiggles are also displayed by most of the other flow variables, as depicted in the accompanying figures.

The typical behavior of the radial velocity of the dispersed phase is displayed in figures 4a and 4b. In the "inviscid" core (u_D/r) is, essentially, a function of time, as predicted by G, and the

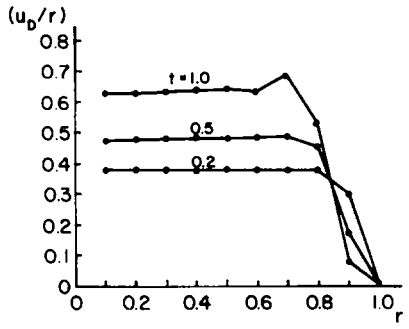

Figure 4a. (u_D/r) vs r at various times; $\alpha = 0.5$. (Numerical results at "midplane" $z = 0.827$.)

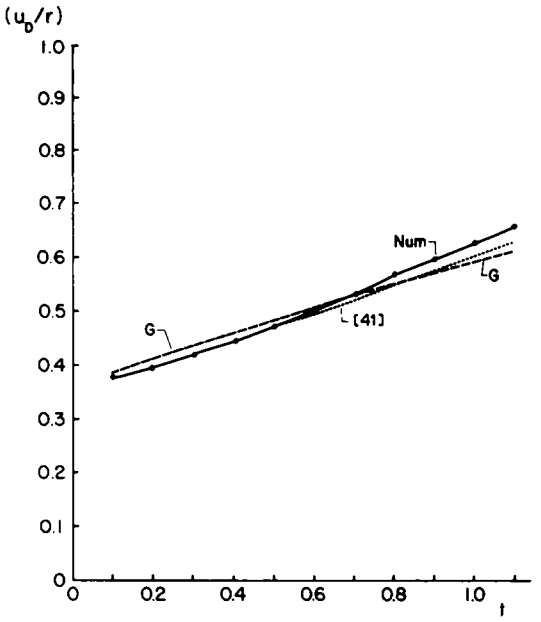

Figure 4b. (u_D/r) vs t in the core; $\alpha = 0.5$. [Numerical results at (0.10, 0.827).]

quantitative agreement between this model and numerical results is good (additional details are given below).

Results for the angular velocity of the mixture core are shown in figures 5a and 5b. (It is recalled that mixture velocities are obtained from the directly computed ε_D, ε_C, $\mathbf{q}_D$ and $\mathbf{q}_C$ variables via the kinematic relationship

$$\mathbf{q}_m = \frac{[(1+\alpha)\varepsilon_D \mathbf{q}_D + \varepsilon_C \mathbf{q}_C]}{(1+\alpha\varepsilon_D)}. \qquad [35]$$

These graphs deserve special attention because they indicate global viscous effects, as follows. First, it is observed that v_m/r decays slightly but monotonically towards $r = 1$. (G and U predict

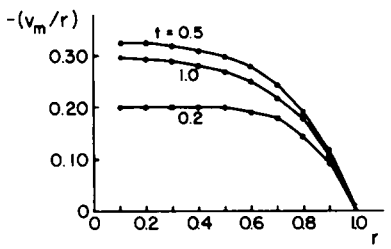

Figure 5a. $-(v_m/r)$ vs r at various times; $\alpha = 0.5$. (Numerical results at "midplane" $z = 0.827$.)

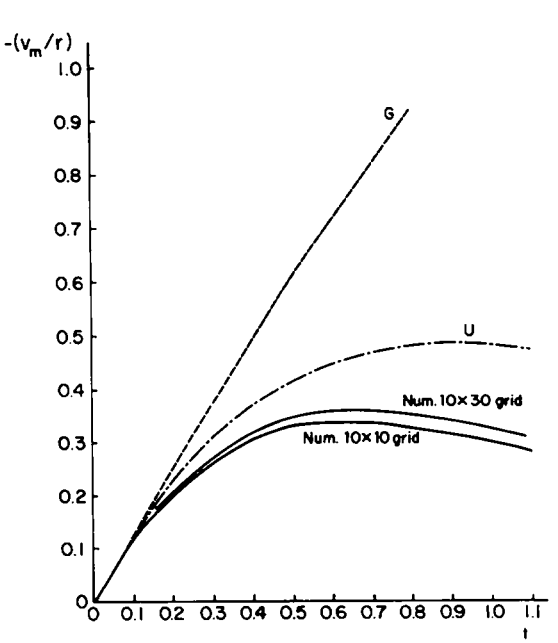

Figure 5b. $(-v_m/r)$ vs t in the core. $\alpha = 0.5$. (Numerical results at closest point to center.)

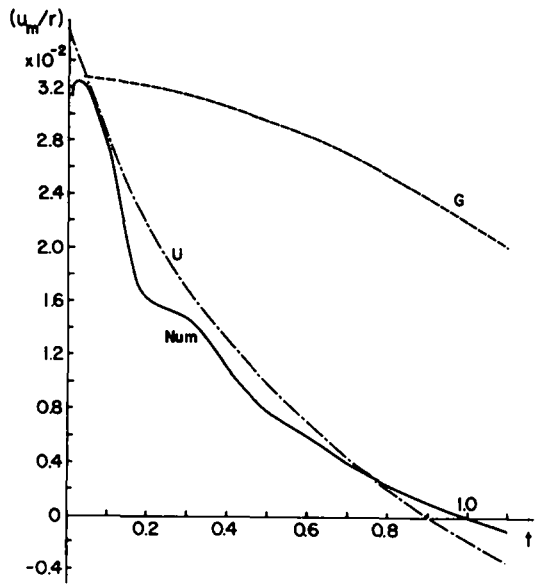

Figure 6. (u_m/r) vs t in the core; $\alpha = 0.5$. [Numerical results at (0.10, 0.827).]

r-independent core values.) This feature can be ascribed to the azimuthal shear on the outer wall which spreads into the interior. Second, but more important, the very pronounced effect of the Ekman layers show up in the time development of (v_m/r), figure 5b (the finer mesh results are also displayed here). The numerical results are both quantitatively and qualitatively different from the prediction of the *infinitely long* cylinder model G. However, the agreement with the *finite* cylinder model U is much better. Moreover, a similar comportment is observed in figure 6. Except for the initial relaxation time, which is neglected in U, and for an oscillation around $t = 0.2$ (whose investigation is not pursued here), the agreement between the quite small numerical values of the secondary variable (u_m/r) and model U is indeed very good.

Viscous effects are also reflected by the axial velocities, for which the numerical results display the following interesting features. The difference $|w_C| - |w_D|$ is usually positive but quite small, typically 2% for $t \leqslant 0.1$ and 0.5% for $t \geqslant 0.2$. w_D is antisymmetric with respect to the midplane $z = 1$. The extremal value is reached at the second meshpoint away from the endplates ($\Delta z = 0.247$) and can be regarded as the Ekman layer suction, subsequently denoted by $\tilde{w}$. Further away from the plates w_D changes linearly. The radial variation of $\tilde{w}$, figure 7a, attests, again, the presence of an r-independent core surrounded by a quite thick viscous region induced by the outer wall and by the sediment layer. Moreover, these profiles emphasize the resemblance of the present two-phase

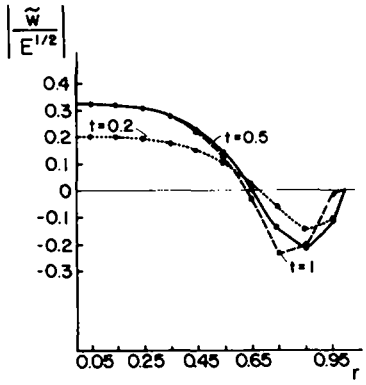

Figure 7a. Ekman suction $(\tilde{w}/E^{1/2})$ vs r at various times; $\alpha = 0.5$. (Numerical results of $-w_D/E^{1/2}$ at $z = 0.247$.)

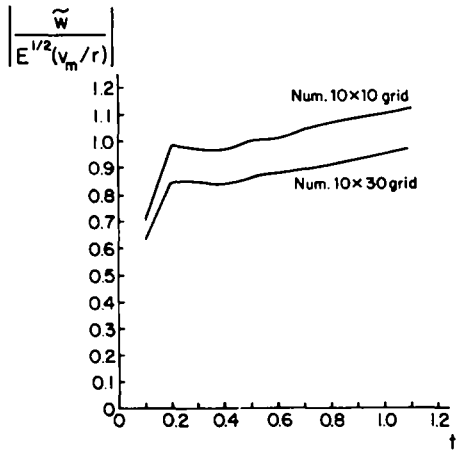

Figure 7b. $(\tilde{w}/E^{1/2})/(v_m/r)$ vs t; $\alpha = 0.5$. [Numerical results at (0.05, 0.247) and (0.05, 0.527) for coarse and fine grids.]

flow to spin-up motions of homogeneous fluids. Thus, the slower fluid is sucked into the Ekman layers where it is transported outwardly and subsequently pumped into the interior near the outer wall. The latter region apparently possesses a shear layer structure, as mentioned above. However, the analytic understanding of the corresponding two-phase flow is presently incomplete and under investigation (Ungarish 1988b). Figure 7b shows that the Ekman layer suction quickly becomes quasi-steady and is simply related to the angular velocity of the core (recall that these layers are expected to develop during a time interval $\sim|\alpha|\beta$, which equals 0.05 in this run). This behavior is in good agreement with the results U and suggests that the Ekman layer suction can be reasonably approximated by the integral correlation

$$\tilde{w}_D = \tilde{w}_C = \pm K E^{1/2}\left(\frac{v_m}{r}\right) \qquad [36]$$

in a wide range of parameters; here K is a coefficient close to 1 and the + and − correspond to $z = 0$ and H, respectively. The correlation [36] proves very useful in the derivation of an improved analytic two-fluid model for the finite cylinder (Ungarish 1988a).

The foregoing results indicate the importance of the shear layers on the endplates $z = 0$, H in establishing the azimuthal, axial and radial velocity components. Although the coarse grid has only three computational points athwart the Ekman layer, the results in the outer region are in very good agreement with those obtained on the fine grid, with about 10 corresponding points, as seen in figures 5b and 7b. This indicates that some of the discrepancies between the numerical results and theory cannot be attributed to discretization errors, but are apparently more intrinsic. The main factor is, probably, the presence of the sublayer of larger ε_D. Here the radial buoyancy force is obviously stronger than accounted for by the analytic model, cf. appendix D, and the radial velocity near the plate is enhanced accordingly. Additional disagreements are introduced by the higher-order terms in the asymptotic theory. For instance, $\alpha\varepsilon_D$ and $E^{1/2}$, both attached with higher negligibly small terms in model U, are actually equal to 0.1 in the run data of case I. Furthermore, the shear on the outer wall, also neglected in that model, clearly shows up in the numerical solution. Consequently, it can be argued that the numerical errors in (v_m/r) and in w_D are not larger than, say, 15%. In this respect, it is worthwhile mentioning again that the numerical results for (u_m/r) are encouraging in the sense that important effects have not been deteriorated by the numerical errors. This variable, sensitive to the Ekman layers and of typical magnitude 10^{-2}, has been obtained from the computed $O(1)$ values of ε_D, ε_C, u_C and u_C via the algebraic formula [35]. Despite the expected error amplification due to cancellation of leading terms, the results compare very satisfactorily with theory, cf. figure 6.

Attention is focused now on the components of the relative velocity, $\mathbf{q}_R = \mathbf{q}_D - \mathbf{q}_C$. This variable deserves special concern for the following reasons: (a) it is the dominant factor in phase separation; (b) its calculation is a major motivation for using the two-fluid formulation instead of the apparently simpler "mixture" model, which relies on a closure assumption for $\mathbf{q}_R$; (c) it decays to zero via the sublayer; and (d) contrary to initial expectations, it may be considerably affected by the Ekman layers on the endcaps. It is recalled that $\mathbf{q}_R \cdot \hat{z}$ is negligible.

The typical axial variation of $\mathbf{q}_R$ is depicted in figure 8c. Here again, the sublayer is observed. Some understanding of the driving balance in this region is gained as follows. Eliminating the pressure term from [15] and [16] and considering the limit of small α, β and E, yields the approximation

$$0 = \frac{\alpha}{|\alpha|}\frac{1}{\beta} r\hat{r} - \frac{1}{\beta}\frac{D(\varepsilon_D)}{1-\varepsilon_D}\mathbf{q}_R + E\frac{\partial^2}{\partial z^2}\mathbf{q}_R,$$

subject to $\mathbf{q}_R = 0$ at $z = 0$ and decay of the viscous term for large z. If ε_D is assumed z independent, one gets

$$\mathbf{q}_R = \frac{\alpha}{|\alpha|}\frac{1-\varepsilon_D}{D(\varepsilon_D)} r\hat{r}\left\{1 - \exp\left[-\frac{z}{\sqrt{E\beta\dfrac{1-\varepsilon_D}{D(\varepsilon_D)}}}\right]\right\}. \qquad [37]$$

Next, combining [13] and [14] and using kinematic relationships yields

$$\frac{\partial \varepsilon_D}{\partial t} + [\mathbf{q}_C + (1-\varepsilon_D)\mathbf{q}_R] \cdot \nabla \varepsilon_D = -\varepsilon_D(1-\varepsilon_D)\nabla \cdot \mathbf{q}_R,$$

whose characteristic solution, on account of [37], is

$$\frac{d\varepsilon_D}{dt} = -2\frac{\alpha}{|\alpha|}\varepsilon_D \frac{(1-\varepsilon_D)^2}{D(\varepsilon_D)}\left\{1 - \exp\left[-\frac{z}{\sqrt{E\beta \dfrac{1-\varepsilon_D}{D(\varepsilon_D)}}}\right]\right\}. \qquad [38]$$

The foregoing crude approximations reveal both the formation of the sublayer of thickness $\sim\sqrt{E\beta}$ and the fact that ε_D decays considerably slower in it, with $(d\varepsilon_D/dt)\to 0$ as $z\to 0$. (A similar behavior shows up, obviously, near $z = H$.) It is anticipated that the axial variation of ε_D becomes ultimately steeper with tendency towards a jump from 0 to $\varepsilon_D(0)$ at $z = 0$ as $t\to\infty$. This resembles the singularity $\partial\varepsilon_D/\partial z\to\infty$ detected in the steady-state von Karman layer (Ungarish & Greenspan 1983). However, no such difficulty was encountered during the time interval computed here.

Outside the thin sublayer, $\mathbf{q}_R$ is strongly z independent. Moreover, figures 8a and 9a indicate that both (u_R/r) and (v_R/r) are functions of t only in the core region, in agreement with G. This supports the hypothesis that outside the sublayer the relative velocity is established by local balances between buoyancy, Coriolis and drag, irrespective of boundary conditions. Consequently, the quite significant and monotonically increasing discrepancy with the results of G, cf. figures 8b and 9b, is, at the first glance, surprising. However, it is argued that these are, essentially, not numerical errors—but rather a by-product of the lack of Ekman layers in solution G. The local balances

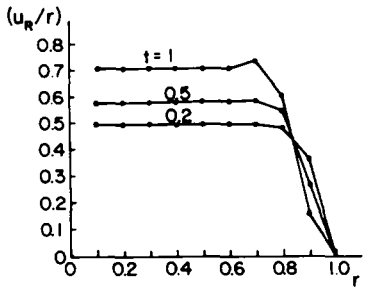

Figure 8a. Relative radial velocity (u_R/r) vs r at various times; $\alpha = 0.5$. (Numerical results at "midplane" $z = 0.827$.)

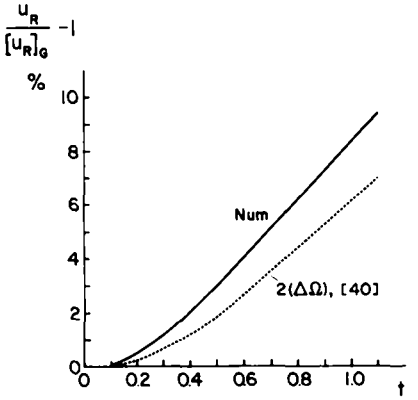

Figure 8b. For (u_R/r), percentage discrepancy with model G vs t; $\alpha = 0.5$. [Numerical results at (0.10, 0.827).]

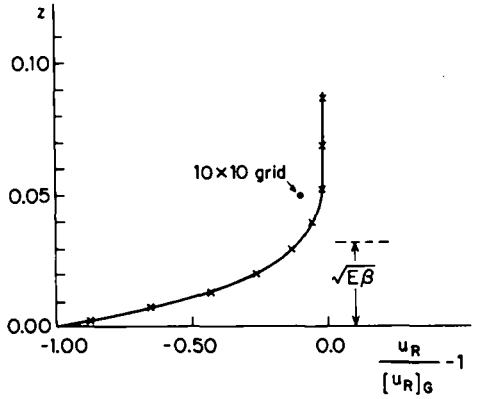

Figure 8c. Relative radial velocity vs z in the sublayer, at $t = 0.2$, $r = 0.10$. ×, 10 × 30 grid (values of z_j can be inferred from the graph); ●, 10 × 10 grid (at closest point to boundary).

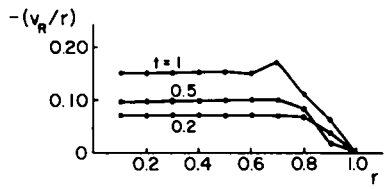

Figure 9a. Relative azimuthal velocity (v_R/r) vs r at various times; $\alpha = 0.5$.

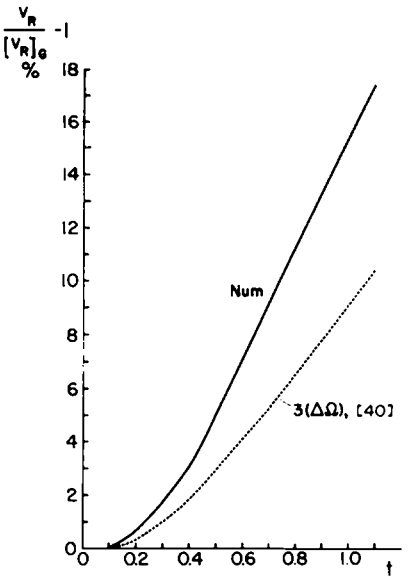

Figure 9b. For (v_R/r), percentage discrepancy with model G vs t. [Numerical results at (0.10, 0.827).]

between centrifugal buoyancy and drag in the radial direction and between Coriolis and drag in azimuthal direction yield

$$u_R \propto \Omega_{eff}^2 \tag{39a}$$

and

$$v_R \propto \Omega_{eff} u_R \propto \Omega_{eff}^3. \tag{39b}$$

Here, the dimensionless effective angular velocity of the mixture is

$$\Omega_{eff} \approx 1 + |\alpha|\beta\left(\frac{v_m}{r}\right). \tag{39c}$$

In view of [39c] and figure 5b, the model G underestimates Ω_{eff} by the relative amount

$$\Delta\Omega = |\alpha|\beta\left[\left(\frac{v_m}{r}\right)_U - \left(\frac{v_m}{r}\right)_G\right], \tag{40}$$

where U and G refer to the appropriate analytic models. According to [39], u_R and v_R of model G require the corrections $2(\Delta\Omega)$ and $3(\Delta\Omega)$, which, as shown in figures 8b and 9b are in reasonable agreement with the numerical results. It is therefore concluded that the numerical error is only in the range of 3% in u_R and 6% in v_R. In fact, a similar correction should be applied to the calculation of $\varepsilon_D(t)$ by model G, cf. figure 3b. The corrected values, not shown here, indicate that the numerical error in ε_D is even less than 1%.

In the same spirit, it can be shown (Ungarish 1988a) that an improved analytic approximation for u_D is

$$[u_D]_{improved} = [\mathbf{j}_m \cdot \hat{r}]_U + [(1 - \varepsilon_D)u_R]_G(1 + 2\,\Delta\Omega). \tag{41}$$

Therefore, in view of figure 4b, it is claimed that the numerical error in u_D is less than 0.5%.

It is noted in passing that case I was also solved with $\sigma_D = 0.2$, on the 10×30 mesh. No major modification of the flow field, as compared to the original $\sigma_D = 1$ run, was observed. The details are omitted for brevity.

Similar numerical results were obtained for system II. The values of $\alpha = 0.1$ and $\lambda = 5$ cause small u_m and v_m, which motivated a high resolution run, on a 20×30 grid, with $\delta t = 2 \times 10^{-5}$.†

†The axial spacing is identical with that of figure 3c, and the radial points are equally spaced. Each time step required 0.13 CPU s on a CRAY X-MP/48.

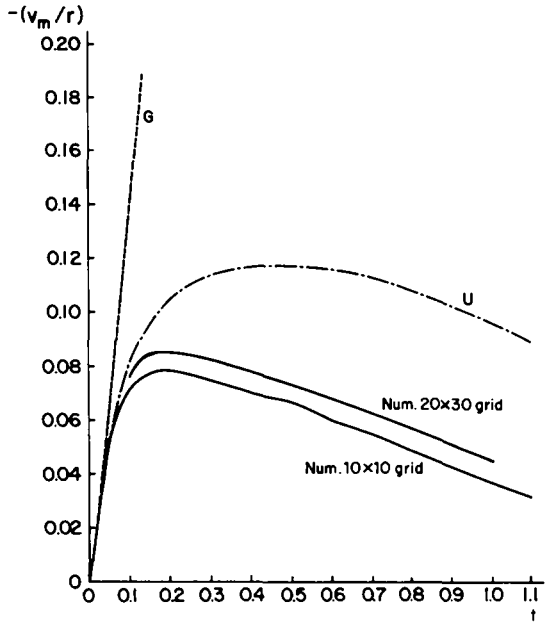

Figure 10. Same as figure 5b, for $\alpha = 0.1$.

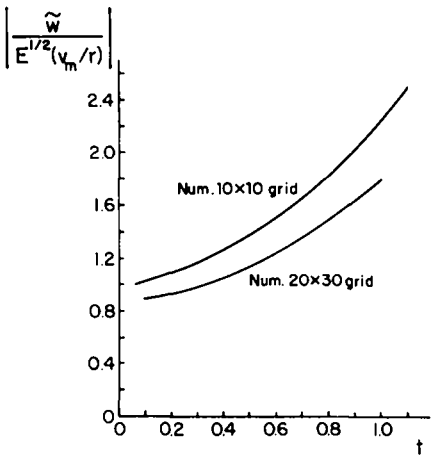

Figure 11. Same as figure 7b, for $\alpha = 0.1$.

The essential flow features discussed above carry over to system II—subject to quantitative differences due to the significantly smaller α. Figure 10 shows a dramatic deviation of the angular velocity from solution G, reflecting the dominant influence of the Ekman layers as indeed expected for the present $\lambda = 5$. However, the Ekman suction exhibits a continuous drift from correlation [36], see figure 11. This unexpected behavior can be attributed to the contribution of the sublayer whose relative importance ultimately increases when $|v_m/r|$ is small, cf. appendix D. The discrepancy between the numerical results and model U observed in figure 10 is mainly explained by the same argument, but the contribution of the side wall shear may also be important in accelerating the decay of the angular velocity.

5. CONCLUDING REMARKS

A finite-difference solver for the full two-fluid equations of motion in a rotating finite axisymmetric cylinder has been developed and verified via a comparison with previous analytic approximations. On a quite coarse grid (10×10 intervals and only three points across the Ekman layer), the representative estimates for the numerical errors are: 1% for the primary variables u_f and ε_f; 5% for the relative velocities u_R and v_R; and 15% for the secondary variables v_m and w_f (here f denotes phases D or C). A typical run requires $\sim 10/|\alpha|\beta^2$ time steps and for each one the major computational effort is dedicated to the solution of a Poisson-type equation for the pressure.

This investigation suggests several requests for improvement of the numerical scheme, such as damping of the spatial oscillations near the sediment layer, and more important, the implicit treatment of the drag terms to alleviate the present numerical stability restriction $\delta t < |\alpha|\beta^2/D(\varepsilon_D)$. In addition, it seems that performance on supercomputers can be considerably enhanced by implementing special vector routines and multitasking in the solution. For example, after calculating the "new" pressure P_{ij}^+, the remaining flow variables for phases D and C can be computed simultaneously (cf. Larson 1984).

The numerical solutions display peculiar sublayers of thickness $\sim\sqrt{E\beta}$ ($\sim$ one dispersed particle radius in dimensional form) beneath the more conventional Ekman layers on the endcaps. In these sublayers the mixture separates considerably slower than in the outer region, and the enhanced buoyancy increases the apparent suction of the Ekman layers. The possibility of such sublayers was pointed out by Ungarish & Greenspan (1983), and, to the best of the author's knowledge, this

is the first numerical solution of the full equations of motion which confirms that prediction. However, the physical interpretation of this result is obscure and requires experimental support, see also the discussion in the above-mentioned paper. Fortunately, there are indications that, in the present problem, the main numerical solution is essentially unaffected by the resolution of this very thin region.

Notwithstanding the sublayer, the present numerical results increase confidence in the previous analytic investigations of the flow field in a cylinder. Greenspan's (1983) solution property reproduces ε_f, u_f, u_R and v_R. Ungarish's (1986) model approximates well the Ekman layers influence on v_m and u_m. Furthermore, these two models can be combined to yield improved analytic values for u_R and v_R, a topic which has been pursued by Ungarish (1988a). These conclusions are expected to be relevant to the parameter range $|\alpha| \leqslant 1$, $E \ll 1$, $\beta \ll 1$, $H \gg E^{1/2}$, $\varepsilon_D \leqslant 0.5$.

The numerical runs also indicate an interesting shear layer structure adjacent to the sediment layer on the outer wall, a topic worthy of further investigation (Ungarish 1988b).

However, it is emphasized again that the two-phase formulation used in the present solution and in the above-mentioned previous analytic studies contains several critical assumptions, such as the stress term postulate, the linear drag law and the no-slip boundary conditions. It is very encouraging to find that the resulting equations yield consistent and, apparently, physically meaningful flow patterns in the difficult non-intuitive regime under consideration. These results can serve as a good starting point and motivation for experimental verifications. In this respect, it is noted that different boundary and initial† conditions, stress terms, drag laws and shear-lift forces can be straightforwardly incorporated in the present numerical solver—which, in this respect, has a considerable advantage over the less versatile analytical models.

Acknowledgements—Mrs A. Berkman performed most of the sophisticated programming and assisted in the analysis of the results. The author also wishes to thank Professor H. P. Greenspan and Dr G. Pinchuk for stimulating discussions. This research was partially supported by NSF Grant No. 8519764 DMS, which provided access to the CRAY-X MP at the Pittsburgh Supercomputing Center, and by Edelstein Research Fund Grant No. 120-0670.

REFERENCES

AMBERG, G. & DAHLKILD, A. A. 1987 Sediment transport during unsteady settling in an inclined channel. *J. Fluid Mech.* **185,** 415–436.

CARVER, M. B. 1984 Numerical computation of phase separation in two-fluid flow. *J. Fluids Engng* **106,** 147–153.

DREW, D. A. 1983 Mathematical modeling of two-phase flow. *A. Rev. Fluid Mech.* **15,** 261–291.

GREENSPAN, H. P. 1983 On centrifugal separation of a mixture. *J. Fluid Mech.* **127,** 91–101.

HARLOW, F. H & AMSDEN, A. A. 1971 A numerical fluid dynamics method for all speeds. *J. comput. Phys.* **8,** 197–205.

ISHII, M. 1975 *Thermo-fluid Dynamic Theory of Two-phase Flow*. Eyrolles, Paris.

ISHII, M. & ZUBER, N. 1979 Drag coefficient and relative velocity in bubbly, droplet or particle flows. *AIChE Jl* **25,** 843–854.

ISSACSON, E. & KELLER, H. B. 1966 *Analysis of Numerical Methods*. Wiley, New York.

LARSON, J. L. 1984 Multitasking on the CRAY X-MP-2 multiprocessor. *Computer (IEEE)* **17,** 62–69.

PROSPERETTI, A. & JONES, A. V. 1984 Pressure forces in disperse two-phase flow. *Int. J. Multiphase Flow* **10,** 425–440.

TOREN, M. & SOLAN, A. 1979 Laminar compressible flow over a stationary disk in a rotating cylinder. *Trans. ASME Jl Fluids Engng* **101,** 173–180.

UNGARISH, M. 1986 Flow of a separating mixture in a rotating cylinder. *Phys. Fluids* **29,** 640–646.

UNGARISH, M. 1988a Two-fluid analysis of centrifugal separation in a finite cylinder. *Int. J. Multiphase Flow* **14,** 233–243.

†For example, the practical spin up from rest is expected to be different from the present solution when λ is not large.

UNGARISH, M. 1988b Side wall effects in centrifugal separation of mixtures. *Phys. Fluids.* Submitted.

UNGARISH, M. & GREENSPAN, H. P. 1983 On two-phase flow in a rotating boundary layer. *Stud. appl. Math.* **69,** 145–175.

UNGARISH, M. & GREENSPAN, H. P. 1984 On centrifugal separation of particles of two different sizes. *Int. J. Multiphase Flow* **10,** 133–148.

APPENDIX A

Greenspan's (1983) *infinitely long* cylinder solution for the mixture zone follows from the similarity assumptions $\varepsilon_f = \varepsilon_f(t)$, $\mathbf{q}_f = r[U_f(t)\hat{r} + V_f(t)\hat{\theta}]$ and $P = r^2 P(t)$, where $f = \mathrm{D}$ or C.

Substitution into [13]–[19] yields, after some arrangement and elimination of P from the radial equations:

$$\varepsilon_D U_D + \varepsilon_C U_C = 0, \tag{A.1}$$

$$\varepsilon_D' + 2\varepsilon_D U_D = 0, \tag{A.2}$$

$$\beta(1+\alpha)[\beta|\alpha|(V_D' + 2U_D V_D) + 2U_D] = D(\varepsilon_D)(V_C - V_D), \tag{A.3}$$

$$\beta[\beta|\alpha|(V_C' + 2U_C V_C) + 2U_C] = -\frac{\varepsilon_D}{1-\varepsilon_D} D(\varepsilon_D)(V_C - V_D) \tag{A.4}$$

and

$$u_D' = \frac{1-\varepsilon_D}{1+\alpha(1-\varepsilon_D)}\left\{\frac{2\varepsilon_D U_D(U_D - U_C)}{1-\varepsilon_D} + U_C^2 - V_C^2 - (1+\alpha)(U_D^2 - V_D^2) + \frac{2}{\beta|\alpha|}\left[(1+\alpha)V_D - V_C\right] + \frac{1}{\beta^2|\alpha|}\left[\frac{\alpha}{|\alpha|} + \frac{D(\varepsilon_D)}{1-\varepsilon_D}(U_C - U_D)\right]\right\}; \tag{A.5}$$

with the initial conditions $\varepsilon_D = \varepsilon_D(0)$, $U_f = V_f = 0$. This system is integrated by standard methods. It is worth noting that E and H do not enter this formulation (because the viscous terms are identically zero), and that [A.1] asserts $\mathbf{j}_m \cdot \hat{r} \equiv 0$.

APPENDIX B

Ungarish's (1986) *finite* cylinder model is obtained from the "mixture" formulation and the postulate

$$\mathbf{q}_R = s\frac{1-\varepsilon_D}{D(\varepsilon_D)} r\hat{r},$$

where $s = |\alpha|/\alpha$. The volume flux balance in the inviscid core and Ekman layers leads to the following results for the former region:

$$\varepsilon_D = \varepsilon_D(t), \tag{B.1}$$

$$\left(\frac{\mathbf{j}_m \cdot \hat{r}}{|\alpha| r}\right) = \lambda\sqrt{D(\varepsilon_D)}\left(\frac{\beta v_m}{r}\right), \tag{B.2}$$

$$\left(\frac{u_m}{|\alpha| r}\right) = \frac{\varepsilon_D(1-\varepsilon_D)^2}{D(\varepsilon_D)} + \left(\frac{\mathbf{j}_m \cdot \hat{r}}{|\alpha| r}\right), \tag{B.3}$$

$$\varepsilon_D' = -2s\frac{\varepsilon_D(1-\varepsilon_D)^2}{D(\varepsilon_D)} \tag{B.4}$$

and

$$\left(\frac{\beta v_m}{r}\right)' = -2\lambda\sqrt{D(\varepsilon_D)}\left(\frac{\beta v_m}{r}\right) - |\varepsilon_D'|; \tag{B.5}$$

the prime denotes differentiation in t.

Equations [B.4] and [B.5] are readily integrated with the initial conditions $\varepsilon_D(0)$, $(v_m/r) = 0$. It is observed that E and H enter the formulation via $\lambda = E^{1/2}/|\alpha|\beta H$. The resulting ε_D does not require "corrections" in the Ekman layers, in constrast to v_m and u_m.

A slight inconsistency is noted: the $\sqrt{D(\varepsilon_D)}$ term above apparently corresponds to $\sigma_f = D(\varepsilon_D)$ in [12], but the numerical solution used $\sigma_f = 1$. This implies that the model treats a slightly more viscous fluid in the Ekman layer. On the other hand, the numerical viscosity acts as a compensator of this discrepancy.

APPENDIX C

Consider the vector equation for **J**:

$$\mathbf{J} + 2m\hat{z} \times \mathbf{J} = \mathbf{B}. \tag{C.1}$$

It can be verified by substitution that the solution is

$$\mathbf{J} = \frac{1}{1+4m^2}[\mathbf{B} + 4m^2(\hat{z} \cdot \mathbf{B})\hat{z} - 2m\hat{z} \times \mathbf{B}]. \tag{C.2}$$

Consequently, in the cylindrical coordinates (r, θ, z), one gets

$$\nabla \cdot \mathbf{J} = \nabla \cdot \frac{\mathbf{B}}{1+4m^2} + \frac{\partial}{\partial z}\frac{4m^2 B_z}{1+4m^2} + \hat{z} \cdot \nabla \times \frac{2m\mathbf{B}}{1+4m^2}, \tag{C.3}$$

where the vector identity

$$\nabla \cdot \mathbf{a} \times \mathbf{b} = \mathbf{b} \cdot (\nabla \times \mathbf{a}) - \mathbf{a} \cdot (\nabla \times \mathbf{b}) \tag{C.4}$$

has been employed. Equations [22] and [23] consist of a particular case of the form

$$\mathbf{B} = \mathbf{G} - e\left(\frac{\partial P}{\partial r}\hat{r} + \frac{\partial P}{\partial z}\hat{z}\right), \tag{C.5}$$

with

$$\frac{\partial}{\partial \theta}\mathbf{G}, \qquad \frac{\partial}{\partial \theta}e \qquad \text{and} \qquad \frac{\partial}{\partial \theta}P$$

identically zero.

Substitution into [C.3] yields

$$\nabla \cdot \mathbf{J} = -\frac{1}{r}\frac{\partial}{\partial r}r\frac{e}{1+4m^2}\frac{\partial P}{\partial r} - \frac{\partial}{\partial z}e\frac{\partial P}{\partial z} + \frac{1}{r}\frac{\partial}{\partial r}r\frac{1}{1+4m^2}(G_r + 2mG_\theta) + \frac{\partial}{\partial z}G_z. \tag{C.6}$$

APPENDIX D

An analytic estimate of the Ekman layer flow and its reaction to the increased buoyancy in the sublayer is derived. Let u^I, v^I and p^I denote the known appropriate mixture variables in the inviscid core, and symbols with tildes represent the boundary layer corrections. The sublayer is represented by the einsatz $\tilde{\varepsilon}_D = (\varepsilon_D(0) - \varepsilon_D^I)e^{-\zeta/\sqrt{k\beta}}$, where $\zeta = z/E^{1/2}$, the superscript I denotes the inviscid core and k is a time-dependent decaying function initially of order unity. E, α and β are assumed small. The boundary layer approximations for the linear momentum equations yields

$$-2\tilde{v} = \frac{\partial^2 \tilde{u}}{\partial \zeta^2} + \frac{\alpha}{\beta}[\varepsilon_D(0) - \varepsilon_D^I(t)]e^{-\zeta/\sqrt{k\beta}}r, \tag{D.1}$$

$$2\tilde{u} = \frac{\partial^2 \tilde{v}}{\partial \zeta^2} \tag{D.2}$$

and

$$\tilde{p} = 0. \tag{D.3}$$

Accounting for the boundary conditions, the solution is

$$\tilde{u} = e^{-\zeta}(\mathrm{A}\sin\zeta + \mathrm{B}\cos\zeta) - Be^{-\zeta/\sqrt{k\beta}}, \qquad [D.4]$$

$$\tilde{v} = e^{-\zeta}(\mathrm{A}\cos\zeta - \mathrm{B}\sin\zeta) - 2k\beta Be^{-\zeta/\sqrt{k\beta}}, \qquad [D.5]$$

where

$$\mathrm{A} = -v^1 + 2k\beta B,$$

$$\mathrm{B} = -u^1 + B,$$

$$B = \frac{k}{1 + (2k\beta)^2}\alpha[\varepsilon_{\mathrm{D}}(0) - \varepsilon^1_{\mathrm{D}}(t)]r. \qquad [D.6]$$

The reduced radial volume transport in the Ekman layer is

$$E^{1/2}\int_0^\infty \tilde{u}\,\mathrm{d}\zeta = \tfrac{1}{2}(\mathrm{A} + \mathrm{B}) - \sqrt{k\beta}B \approx \tfrac{1}{2}(-v^1 + B), \qquad [D.7]$$

where the last approximation accounts for $|u^1| \ll |v^1|$ and $k\beta \ll 1$.

The "strength" of the sublayer is reproduced by the buoyancy parameter B, and for $B = 0$ the result of U is recovered. However, the foregoing solution clearly indicates that the additional buoyancy in the sublayer *enhances* the volume transport and *increases* the peak value of u in the Ekman layers. The trend is consistent with the results of figures 5b and 10 in both qualitative and quantitative aspects.